Title
Sulfur Biogeochemical Cycling and Redox Dynamics in a Shale-Dominated Mountainous Watershed

Journal
Journal of Geophysical Research Biogeosciences, 127(6)

ISSN
2169-8953

Authors
Fox, Patricia M
Carrero, Sergio
Anderson, Cam
et al.

Publication Date
2022-06-01

DOI
10.1029/2021jg006769

Sulfur Biogeochemical Cycling and Redox Dynamics in a Shale-Dominated Mountainous Watershed

Patricia M. Fox[1], Sergio Carrero[1], Cam Anderson[2], Christian Dewey[3], Marco Keiluweit[2], Mark Conrad[1], Hannah R. Naughton[3†], Scott Fendorf[3], Rosemary Carroll[4], Baptiste Dafflon[1], Helen Malenda-Lawrence[5], Dipankar Dwivedi[1], Benjamin Gilbert[1], John N. Christensen[1], Kristin Boye[3], Curtis Beutler[6], Wendy Brown[6], Alexander Newman[6], Roelof Versteeg[7], Kenneth H. Williams[1], and Peter S. Nico[1]

[1]Earth and Environmental Sciences Area, Lawrence Berkeley National Lab, 1 Cyclotron Road, Berkeley, CA 94720. [2]University of Massachusetts. [3]Stanford University. [4]Desert Research Institute, [5]Colorado School of Mines, [6]Rocky Mountain Biological Laboratory, [7]Subsurface Insights

Corresponding author: Patricia M. Fox (pmfox@lbl.gov)

†Current address: Earth and Environmental Sciences Area, Lawrence Berkeley National Lab, 1 Cyclotron Road, Berkeley, CA 94720

Key Points:

- Bedrock shale weathering profiles show pyrite oxidation to elemental S and sulfate, with reprecipitation of pyrite at fracture surfaces
- Organic-S compounds dominate S speciation in unsaturated hillslope soil and floodplain sediment
- River corridor processes, such as biological uptake and reduction may attenuate sulfate releases from oxidative pyrite weathering

Abstract

Sulfur (S) is an essential macronutrient and important component of the earth's crust, and its cycling has critical impacts on trace metal mobility, water quality, and human health. Pyrite weathering is the primary pathway by which sulfur enters surface waters. However, biogeochemical cycling of sulfur in soils and the river corridor mediates sulfate exports. In this study, we identified the major forms of sulfur across multiple compartments and scales in a pristine mountainous watershed, including shale bedrock weathering profiles, hillslope soils, and alluvial floodplain sediments, in order to provide insight into biogeochemical sulfur cycling in a hydrologically variable alpine system. X-ray absorption near-edge spectroscopy (XANES) analysis of shale weathering profiles showed clear evidence of pyrite oxidation to sulfate, with large accumulations of intermediate S(0) (20-53%). Micro-scale XANES showed evidence of reprecipitation of pyrite at fracture surfaces within the permanently saturated zone. Organic sulfur dominated S speciation in shallow hillslope soil and floodplain sediment, with little evidence of reduced inorganic S. However, mackinawite formation, representing active sulfate reduction, was observed in saturated oxbow sediments and saturated weathered shale underlying floodplain sediments. Further evidence of sulfate reduction from aqueous sulfur isotopic analysis was observed in shallow groundwater transects across an Fe-reducing meander, whereas increases in pore water sulfate concentrations implied sulfur oxidation at other locations. The data present an integrated picture of sulfur cycling in a shale-dominated watershed, where riverine sulfate exports are mediated by biological cycling, particularly in redox-stratified and temporally dynamic hyporheic zone sediments.

Plain Language Summary

Sulfur is an essential macronutrient and biologically important component of the earth's crust, and its cycling has critical impacts on water quality and human health. Weathering of the mineral pyrite from rock is the primary pathway by which sulfur enters surface waters, and alterations to the hydrologic cycle due to climate change may affect pyrite weathering rates. However, biological cycling of sulfur in soils and the river corridor mediates the release of sulfur to rivers and the ocean. In this study, we identified the major forms of sulfur across a pristine mountainous watershed, including shale bedrock weathering profiles, hillslope soils, and alluvial floodplain sediments. Shale weathering profiles showed pyrite conversion to sulfate, with large accumulations of intermediate elemental sulfur. In the river corridor, precipitation of the mineral mackinawite was observed in water-saturated sediments. By contrast, organic sulfur compounds were the primary forms of sulfur in shallow, unsaturated hillslope soil and floodplain sediment, demonstrating the importance of biological sulfur cycling in these zones. The data present an integrated picture of sulfur cycling in a shale-dominated watershed, where riverine sulfate exports are controlled by a balance of rock weathering and biological cycling, particularly in the hydrologically and biologically dynamic river corridor.

1. Introduction

Sulfur (S) is an essential macronutrient for all forms of life, and a biogeochemically significant constituent of the Earth's crust. Sulfur exists in a wide range of oxidation states ranging from -2 to +6, and a number of organic and inorganic sulfur compounds exist. Pyrite, FeS_2, is the most abundant sulfide mineral and can be found in metamorphic and sedimentary rock formations. The oxidative weathering of pyrite is the primary source of dissolved sulfate in watersheds containing abundant hydrothermally altered, pyritic rocks (mineralized watersheds) and can be associated with environmental concerns such as acid rock drainage (Nordstrom, 2009, 2011), the co-release of toxic metals and metalloids (Morrison et al., 2012; Singer et al., 2020), and high salinity (Mermut and Arshad, 1987; Morrison et al., 2012; Tuttle et al., 2014). A growing number of studies have implicated climate change as the root cause of observed increases in alpine freshwater (river and lake) solute concentrations, including sulfate (Lami et al., 2010; Mast et al., 2011; Rogora et al., 2003; Sommaruga-Wögrath et al., 1997; Thies et al., 2007; Todd et al., 2012; Wögrath and Psenner, 1995). Possible explanations for these increases include declining snowpack, which serves to dilute riverine solutes, melting glaciers, increased weathering rates due to warmer temperatures, and increased weathering due to dropping water tables. For example, Todd et al. (2012) observed an increase of 29.1 mg/L in dissolved sulfate per decade in the Upper Snake River. Manning et al. (2013) attributed the increases in dissolved sulfate in the Upper Snake River to climate-change induced falling water tables which exposed previously unweathered pyrite to oxygenated groundwater. However, pyrite weathering is just the first step in the eventual export of sulfate in surface waters.

The active biogeochemical cycling of sulfur in soils and sediments, particularly in floodplain and river corridor systems, ultimately regulates the export of riverine sulfate. Plant uptake and microbial transformations can convert sulfate to organic sulfur compounds. While sulfate minerals (*e.g.*, jarosite and gypsum) are found in some arid environments and mining impacted systems (Nettleton et al., 1982), organic sulfur compounds make up the vast majority of sulfur in most upland soils (Prietzel et al., 2011; Prietzel et al., 2007; Wilhelm Scherer, 2009) emphasizing the importance of biologically mediated sulfur and carbon cycle coupling. In anoxic environments, sulfate reduction coupled to organic matter oxidation results in the formation of low solubility sulfide minerals such as mackinawite, greigite, and pyrite (Rickard and Luther, 2007; Rickard and Morse, 2005). Anoxic environments that are rich in organic carbon, such as riparian wetlands and freshwater lake sediments, have been shown to remove sulfate

from mining-impacted waters through sulfate reduction (Herlihy and Mills, 1985; Ng et al., 2017; Whitmire and Hamilton, 2005).

While a number of studies have examined sulfur speciation and cycling within different ecosystem compartments (*e.g.*, soils, wetlands, lake sediments, and shales), none have utilized a multi-compartment, whole-watershed approach. Due to the inter-connectedness of watershed compartments, such a whole-watershed approach is needed in order to understand and predict the watershed-scale responses (*e.g.*, riverine sulfate export) to climate change-induced perturbations. While recent research has suggested that bedrock pyrite weathering may increase due to climate change, the degree to which sulfate exports will be attenuated by other watershed compartments or processes is currently unknown. In this study, we aim to identify the processes responsible for sulfur oxidation (*i.e.*, pyrite weathering) and retention within a watershed dominated by pyrite-rich bedrock. The East River watershed in the Upper Colorado River Basin, where Mancos shale is the dominant bedrock (Gaskill et al., 1991) serves as our study site. Here, we perform a cross-compartment, multi-scale investigation on the controls over sulfur biogeochemical cycling and export at the watershed-scale. Dissolved sulfate concentrations in the East River vary seasonally from 0.17 to 0.59 mM, with the lowest concentrations occurring annually during the snowmelt-associated peak discharge period and the highest concentrations occurring during baseflow (Winnick et al., 2017). Pyrite weathering from Mancos shale has been implicated as the source of riverine sulfate in the East River (Winnick et al., 2017). In this study, we use x-ray absorption near-edge spectroscopy (XANES) to determine the speciation of sulfur in three major watershed features: shale bedrock, hillslope soil, and floodplain sediment, representing potential sources and sinks for sulfur. The application of x-ray absorption spectroscopy to natural samples can provide information on sulfur redox states and bonding environments (Fleet, 2005; Prietzel et al., 2007; Vairavamurthy, 1998), and thus is a valuable tool for investigating sulfur cycling in natural systems. Aqueous geochemical measurements, including sulfur isotopes, are then used to complement the XANES data to provide insight into the processes underpinning biogeochemical cycling and riverine export of sulfur in a shale-dominated landscape.

2. Materials and Methods

2.1 Field Site Description and Core Sample Collection

The field site is located in a high-elevation, mountainous watershed of the East River located near Gothic, Colorado, USA. The climate is characterized by long cold winters, with short cool summers and a mean annual temperature of 3°C. The majority (~70%) of the precipitation falls as snow, with total

mean annual precipitation of 680 mm. This watershed is the location of the Watershed Function Scientific Focus Area (SFA) led by Lawrence Berkeley National Laboratory (Hubbard et al., 2018). Solid-phase samples for this study include shale, hillslope soils, and floodplain sediment and the sample locations are shown in Figure 1. GPS coordinates and SFA location IDs for all sampling sites can be found in the Supporting Information (Table S1) and in the SFA site locations dataset (Varadharajan et al., 2020).

Shale samples were collected from two locations in the watershed, on a northeast-facing hillslope adjacent to the river at the Lower Montane site (lower hillslope shale, Figure 1B) at an elevation of 2763 m and from a shale outcrop on Gothic Road (outcrop shale, Figure 1A) at an elevation of 2895 m. The hillslope is characterized by approximately 1-m thick soils underlain by weathered and unweathered shale bedrock (Wan et al., 2021). A continuous vertical core to a depth of approximately 10 m below ground surface (bgs) was collected from the lower hillslope using a track-mounted drill rig and a 0.14-m diameter ODEX drilling bit. A shale weathering profile was observed from 1-3 m bgs. Between 2 – 3 m bgs, numerous fractures were observed along with iron oxide discoloration. The sample denoted “Weathered” was subsampled at a depth of 2.7 m from within the weathering region of one such fracture surface. The sample denoted “Pristine” was subsampled from a piece of solid core at a depth of 9 m. At the outcrop shale site, a horizontal core approximately 1-m long was collected from the outcrop (~1-m above the ground surface) using a hand drill with a 24.5-mm diameter diamond drilling bit using water as a drilling fluid. The sample denoted “Top” was taken from the exposed section of the core, which exhibited signs of weathering such as iron oxide discoloration. The samples denoted “Middle” and “Bottom” were subsampled at depths of 40 cm and 80 cm in the core.

Soil samples were collected from two locations on the Lower Montane hillslope at elevations of 2789 and 2763 m, denoted upper and lower hillslope soils, respectively (Figure 1B). The lower hillslope soil core was co-located with the hillslope shale core (collected 1-2 m away). The hillslope is vegetated by grasses, forbs, and shrubs and is representative of a lower montane meadow environment (Falco et al., 2019). Hillslope soils are approximately 1 m thick, and are underlain by weathered and un-weathered shale bedrock (Wan et al., 2021) and are classified as Tilton sandy loam by the USDA. Soil samples were collected in approximately 15-cm increments using a 5 cm diameter soil core sampler (with slide hammer) to a depth of approximately 60 cm in June 2017. Hillslope soil samples were freeze-dried, sieved through a 2-mm sieve, and ground by hand with an agate mortar and pestle.

153 Sediment samples were collected from two floodplain locations in a meandering reach of the
154 East River (Lower Montane Floodplain site and Brush Creek Site) at elevations of 2760 and 2727 m,
155 respectively (Figure 1). Floodplain vegetation is dominated by *mountain willow* with some *American*
156 *dwarf birch*, *Potentilla*, and grasses (Falco et al., 2019). Sediments were collected from two active
157 meanders (Meander C and Meander Z) and the former river channel of a meander cutoff (Meander Y).
158 Cores were collected from Meander C in June 2017 and July 2018 and from Meander Z and Y in June
159 2018. The Meander Y oxbow was cutoff between 2006 and 2011 when water broke through the neck of
160 the meander (dated from historical aerial imagery) and the former river channel has become filled with
161 fine-grained sediment, with pools of stagnant water that persist year-round. The Meander Y sample was
162 collected from a location filled with sediment which was wet, but did not contain standing water at the
163 time of collection. In Meanders C and Z, sediment profiles consist of a layer of fine-grained material (< 2
164 mm) ranging from 20 to 90 cm deep overlaying coarse-grained alluvium (dominated by gravel and
165 cobbles). Alluvial materials are underlain by weathered shale at depth of approximately 1-2 m. Sediment
166 samples were collected in approximately 15-cm increments using a 5 cm diameter soil core sampler
167 (with slide hammer) until coarse alluvium was reached. After reaching coarse alluvium, sediment was
168 sampled using an 8.3 cm diameter bucket auger. Floodplain sediment samples were placed in
169 polyethylene bags, sealed into aluminized BoPET (Biaxially-oriented polyethylene terephthalate, or
170 Mylar^{TM}) bags containing O_2 absorbers (IMPAK^{TM} corporation), shipped to the laboratory, and stored at
171 4°C until processing in order to preserve anaerobic conditions observed in some cores. Sediment
172 samples were then freeze-dried, sieved through a 2-mm sieve, and ground by hand.

173

174

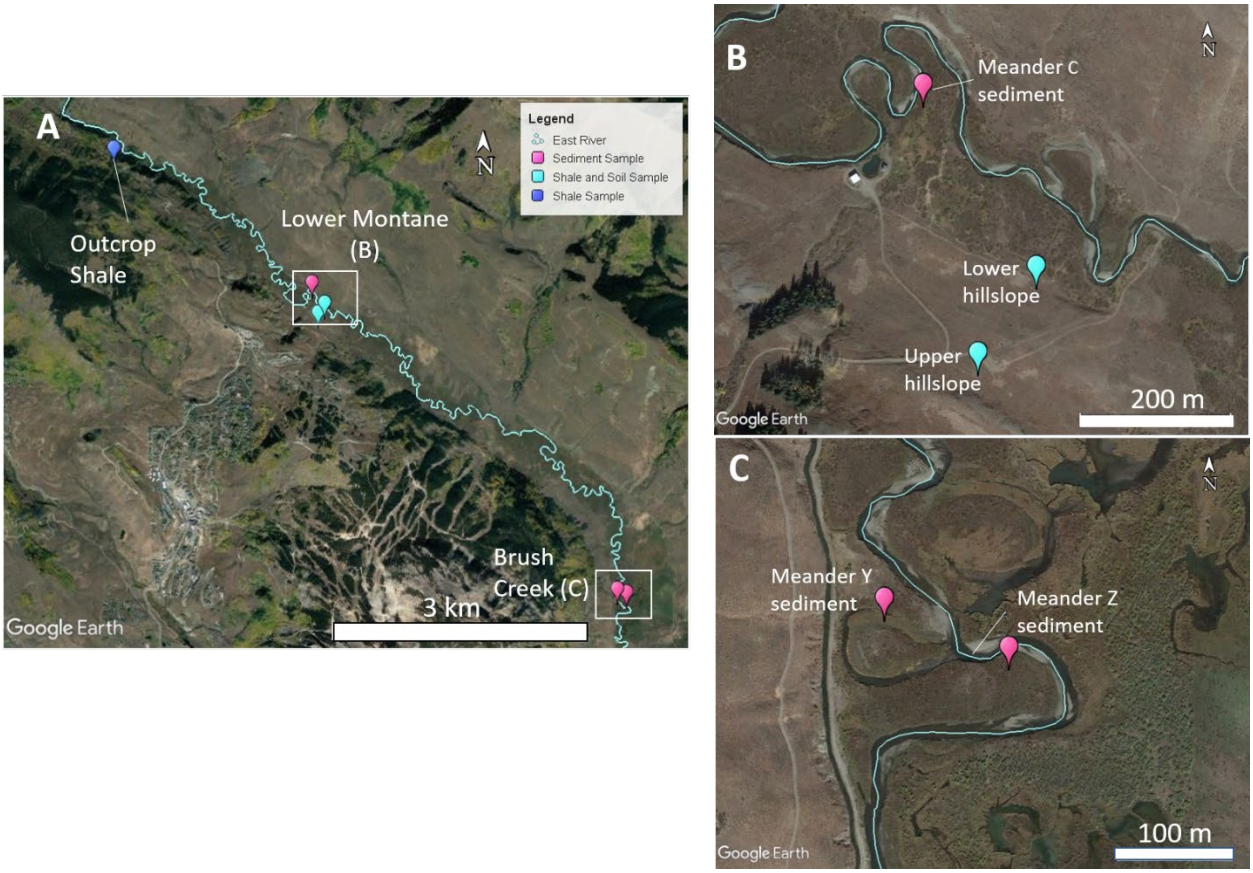

Figure 1. Map showing river reach (A) in the vicinity of the sampling locations for the Outcrop shale core, Lower Montane site (B) and Brush Creek site (C). Sampling locations for soil, sediment, and shale cores are shown. Note that shale and soil samples are co-located in (B).

2.2 Density Fractionations

To isolate sulfur in particulate organic matter, mineral-organic associations, and shale, we employed a density fractionation procedure that relies on a density gradient established in sodium polytungstate solution. Two density cutoffs were chosen to separate soils into (1) a light fraction consisting primarily of particulate organic matter (< 1.6 g cm^{-3}), (2) an intermediate fraction composed of mineral-organic associations [1.6 < x < 2.2 g cm^{-3} (Mikutta et al., 2009)], and (3) a heavy fraction, comprised predominantly of minerals (> 2.2 g cm^{-3}). The fractionation was conducted on 7.5 g of bulk soil by mixing with 30 mL of a low-C and -N sodium polytungstate (SPT-0, Geoliquids Inc., Prospect Hills, IL). Only the light and heavy fractions were analyzed by X-ray absorption spectroscopy.

2.3 Elemental Analysis of Shale

Subsamples from the continuous 10-m core collected at the lower hillslope, including both soil and shale, were analyzed for major and trace element quantification in the laboratory of ALS Global (Reno, NV). Carbon and sulfur were analyzed by combustion and infrared detection according to the

methods C-IR07 and S-IR08, respectively. These data are compared to S profiles at the upper hillslope location from Wan et al. (2021).

2.4 X-ray Absorption Spectroscopy

All samples were analyzed at the sulfur K-edge by x-ray absorption near edge spectroscopy (XANES) at the Canadian Light Source (CLS), Stanford Synchrotron Radiation Laboratory (SSRL), and the Advanced Light Source (ALS). All spectra were recorded in fluorescence mode and the absolute energy position of the sulfur K-edge white line of calcium sulfate was calibrated to 2481.8 eV. Samples analyzed at the SXRMB beamline at the CLS included hillslope and outcrop shale, hillslope soil, and Meander C 2017 sediments, with 2 scans for each sample. The CLS beamline was equipped with a 7-element silicon drift detector. The energy resolution was 0.24 eV. Samples analyzed at beamline 14-3 at SSRL included Meander C 2018 sediments, Meander Y and Meander Z sediments, with 14-19 scans for each sample. No changes in the spectra were observed during data collection. The SSRL beamline was equipped with a 4 element Vortex detector. The energy resolution was 0.24 eV. Microscale X-ray fluorescence (µXRF) imaging and microscale XANES analysis of the hillslope shale were performed using beamline 10.3.2 at the Advanced Light Source. The ALS beamline was equipped with a 1-element silicon drift fluorescence detector and low energy maps were collected at 2700 eV for S, Ca, Si at a 20 × 20 µm and 5 x 5 µm of spot size for lower and higher resolution maps, respectively. The energy resolution was 0.3 eV.

All XANES spectra were processed in Athena (Ravel and Newville, 2005). The energy was calibrated with sulfate using a white line energy of 2481.8 (Fleet, 2005). Multiple scans were averaged, and the pre-edge and post-edge were normalized using linear functions and an edge-step of 1.0. The library of standard spectra was collected at beamline 14-3 at SSRL and the following standards were used for peak identification: mackinawite, natural pyrite, elemental sulfur, methionine, L-cysteine, L-cystine, sodium sulfite, taurine, and iron sulfate. Samples were fit using Athena's linear combination fitting function (LCF). The quality of the fits was evaluated by visual inspection of the model fits and residuals along with the goodness of fit parameters (R factor and reduced chi squared). The model fits and parameters are shown in the SI.

2.5 Groundwater and River Water Data

Groundwater and river water data from the East River watershed have been collected as part of the Watershed Function SFA and the datasets used here are publicly available. Datasets include East River discharge at the pumphouse location (Carroll and Williams, 2019), continuous groundwater elevation data in the Meander C floodplain (Dafflon et al., 2020), dissolved sulfate in river water at the

lower montane (pumphouse) location (Williams et al., 2020), and shallow (< 2 m) groundwater chemistry in the Meander C, Meander D, and Meander Z floodplains (Fox et al., 2021a, Fox et al., 2021b, Fox et al.,2021c). Sulfate $\delta^{34}S$ values were measured on selected groundwater samples using an ECS 4010 Elemental Analyzer coupled to a Delta V^{plus} isotope ratio mass spectrometer. Details of the data collection are described in the datasets and elsewhere (Carroll et al., 2018; Dwivedi et al., 2018). A summary of the water monitoring locations used in this study can be found in Table S2 and Figure S1 in the supporting information.

3. Results and Discussion

3.1 Shale Weathering Profiles

Sulfur speciation in shale samples from two different locations show weathering profiles consistent with pyrite oxidation to sulfate (Figure 2A) as expected. There are two primary peaks in the bulk shale spectra at 2471.4 eV and 2481.8 eV which coincide with the peaks for pyrite and sulfate, respectively. While the position of the sulfur K-edge can vary from 2469.5 to 2475.1 eV for various sulfide minerals, Fleet (2005) found the edge position for pyrite is 2471.5 eV, consistent with the peak observed in our shale samples and pyrite standard. Elemental sulfur, with an edge position of 2471.8 eV, overlaps with the pyrite peak and may also contribute to absorbance in the 2470-2475 eV region. The hillslope shale shows an increase in the sulfate peak at 2481.8 eV from the pristine (9-m bgs) to the weathered (2.7-m bgs) shale sample. The presence of a small sulfate peak in the pristine shale suggests that the pyrite is partially oxidized; this oxidation may have occurred *in situ* or during sample preparation, but is a minor component of the total sulfur signal. The outcrop shale “Top” sample, which was collected from an exposed outcrop of shale, is the most oxidized of all the shale samples showing a large sulfate peak, while the Outcrop shale middle and bottom samples, collected from 40 and 80-cm depth of the shale outcrop, are similar to the hillslope weathered shale sample.

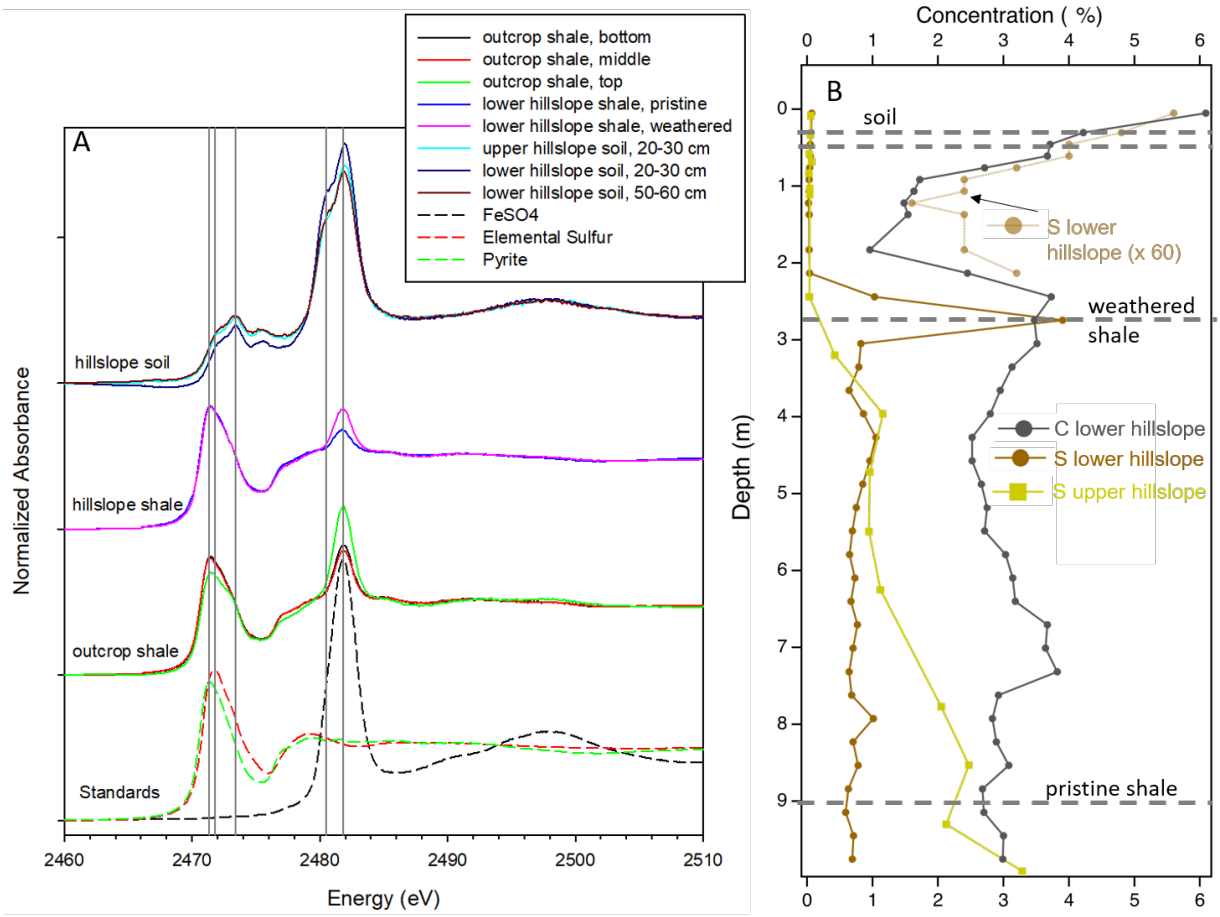

Figure 2. (A) Sulfur K-edge XANES data showing shale weathering profiles for two locations: outcrop shale and lower hillslope shale along with upper and lower hillslope soil. Standard spectra for natural pyrite, elemental sulfur and iron(II) sulfate are also shown. Vertical lines indicate the locations of pyrite, elemental sulfur, reduced organic-S, oxidized organic-S, and sulfate peaks at 2471.4, 2471.8, 2473.4, 2480.5, and 2481.8 eV, respectively. (B) Vertical elemental profiles for S, and C at the upper and lower hillslope locations. Note that for the lower hillslope data, S concentrations are also shown as 60 times the actual concentration for the top 2.2 m, revealing a trend consistent with that of carbon. Horizontal dashed lines indicate the depths of the bulk XANES data in panel (A). Elemental S data for the upper hillslope is from Wan et al. (2021).

Figure 2B shows depth concentration profiles for sulfur and carbon (C) at the upper and lower hillslope. The upper hillslope sample shows a smooth drop in total S concentrations from 4 to ~2.5 m bgs suggesting progressive loss of sulfur due to pyrite oxidation at this relatively oxic, well-drained location. By contrast, the lower hillslope sample shows a large accumulation of sulfur occurring in the weathered shale at 2.7 m bgs (Figure 2B). This accumulation of sulfur in the lower hillslope coincides with the top of

the permanently saturated zone at this location which remains largely anoxic due to the proximity to the river (Wan et al., 2021). This zone in the lower hillslope may serve as a redox barrier, which traps sulfur released from other parts of the watershed (e.g., upper hillslope). While this zone is confined to ~0.5 m thick band, the sulfur concentrations in this band are five times higher than the underlying pristine bedrock.

Figure 3 shows microscale XRF and XANES data collected at a shale fracture at 2.7 m bgs in the lower hillslope shale core which shows the distribution of chemistry in the shale from the fracture surface to the interior of the shale. The chemistry near the fracture can be grouped into three distinct zones: (1) the sulfur pristine zone, which occurs far (~1 cm) from the fracture surface, (2) the sulfur precipitation zone, which occurs directly adjacent to the fracture surface, and (3) the carbonate pristine zone, which sits in between zones (1) and (2). The sulfur pristine zone contains abundant S and Ca, presumably from unweathered pyrite and carbonate minerals, including both calcite and dolomite (Figure 3B). Micro-XANES data confirmed the presence of relatively pristine pyrite in this zone, with a spectrum which closely resembled that of the bulk pristine pyrite collected from 9-m bgs (Figure 3D). In the intermediate zone (carbonate pristine zone), sulfur is almost completely lost, with only a few low concentration spots remaining (Figure 3C), while Ca, representing carbonate minerals, is retained. The sulfur concentrations in this zone were generally too low for μ-XANES analysis, but one location where XANES data collection was feasible revealed very little to no pyrite remaining, with a large sulfate peak and a smaller peak centered at ~2473 eV, which is consistent with reduced organic sulfur. This organic sulfur may represent either microbially processed sulfur or organic sulfur associated with shale kerogen. Directly adjacent to the fracture surface (sulfur precipitation zone), there is a loss of carbonate minerals and the reappearance of a large number of concentrated sulfur spots (Figure 3C). These sulfur spots have large peaks at 2471.4 eV (consistent with the peaks for pyrite and elemental sulfur) and closely resemble the spectra of bulk weathered shale. Given the spatial distribution of sulfur, it is likely that this sulfur represents sulfate which was oxidized from pyrite in other locations (*e.g.*, further upslope or from within the carbonate pristine zone), transported, and subsequently reduced and precipitated at the fracture surface. The high concentrations of sulfur in this weathered shale zone (Figure 2B) coupled with the microscale XRF and XANES data suggest that shale fractures are important zones controlling pyrite weathering and sulfate transport/release. Furthermore, the data reveal that shale weathering is not a unidirectional process, and pyrite-derived sulfur may undergo multiple cycles of oxidation and reduction before being ultimately oxidized and exported from the subsurface as sulfate.

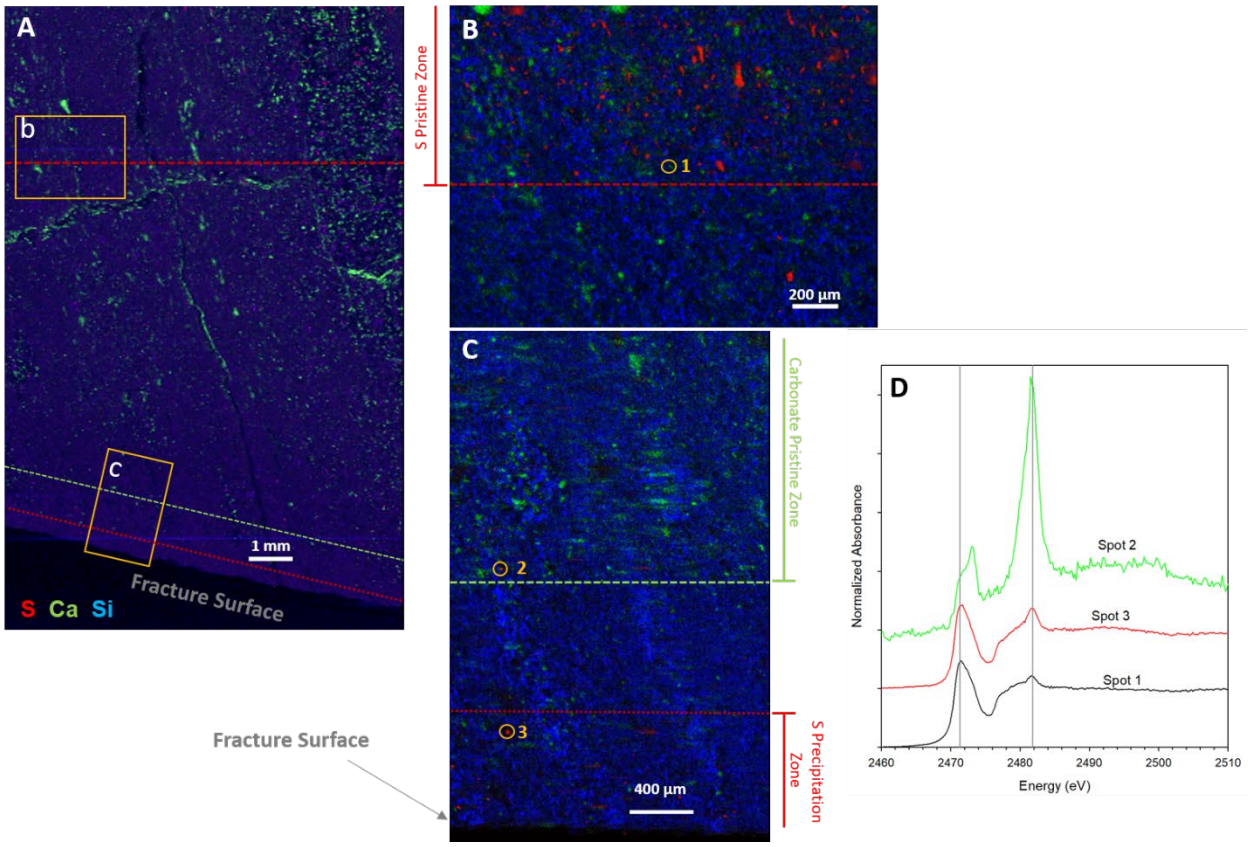

Figure 3. (A) Larger-area µ-XRF map collected on a fracture surface from the hillslope shale core located 2.7 m bgs that showed visual evidence of weathering. Boxes indicate the locations of higher-resolution maps: (B) the sulfide mineral weathering front and (C) fracture surface, including the carbonate mineral weathering front and sulfur precipitation zone; (D) Sulfur µ-XANES spectra collected at the spots indicated in maps (B) and (C). The vertical lines in (D) indicate the energies of pyrite and sulfate at 2471.4 and 2481.8 eV, respectively.

Results of linear combination fitting show that pyrite accounts for 11-69% of the bulk shale sulfur, elemental sulfur made up 20-53%, and sulfate made up 11-36% (Table 1, Figure S2). The pristine hillslope shale sample contains the highest amount of unweathered pyrite at 69 ± 2%, while the exposed shale outcrop (Outcrop Top) sample is the most highly weathered, with only 11 ± 5% pyrite and the largest fractions of both elemental sulfur and sulfate, 53 ± 5% and 36 ± 0.7%, respectively. The other shale samples are very similar to one another, with 45-54% pyrite, 26-34% elemental sulfur, and 17-21% sulfate. The edge positions of pyrite and elemental sulfur are separated by only 0.4 eV, and the two

species are often grouped together as "reduced inorganic sulfur" (*e.g.*, Singer et al., 2020). However, the inclusion of both pyrite and elemental sulfur in the linear combination fitting of our shale spectra improves the fit, most noticeably for the more weathered shale samples (*i.e.*, Outcrop shale, top), better capturing the wider peak at 2470-2475 eV (Figure S2, Table S3). While there is likely some uncertainty in the exact ratio of pyrite to elemental S determined by these fits, the decrease in pyrite and the increase in elemental S and sulfate from pristine to weathered in both shale cores suggests elemental S as an important intermediate in the weathering process. However, it is important to note that reduced inorganic sulfur (primarily elemental S) still makes up the majority of the total S, even in the most highly weathered shale sample analyzed. These observations are consistent with incomplete pyrite oxidation in weathered shale.

There are numerous pyrite oxidation pathways, including abiotic (*e.g.*, by Fe(III) and O_2), direct biotic (S oxidizing bacteria), and indirect biotic (Fe oxidizing bacteria) (Nordstrom, 2000). Oxidation of pyrite-sulfide, with a charge of -1, to sulfate, with a charge of +6, proceeds through multiple steps, with thiosulfate, elemental S, and lower valent sulfoxyanions (*e.g.*, sulfite) as intermediates; however, thiosulfate and sulfite are easily oxidized and short-lived (Nordstrom, 2000) and we do not see evidence of these forms in the XANES spectra. We do, however, see evidence for the accumulation of elemental sulfur that is consistent with the known pyrite oxidation intermediates. Sulfate salts and minerals (*e.g.*, gypsum, jarosite, $FeSO_4$) are highly soluble in water and therefore sulfate can be transported away from the source rock when saturated. Indeed, high concentrations of dissolved sulfate (9-11 mM) are observed in groundwater during the spring and early summer at 2-4 m bgs on the hillslope, while lower dissolved sulfate concentrations (<2 mM) are observed below 4 m in the permanently saturated zone (Wan et al., 2021). The presence of sulfate in the solid shale samples is therefore indicative of incomplete dissolution due to insufficient leaching relative to the rate of oxidation or physical isolation of the sulfate species from the leaching water. Changes in hydrologic conditions will likely impact the rate and timing of sulfate release even within the oxic shale weathering zone.

Table 1. Results of linear combination fitting of shale sulfur spectra showing percent contribution from pyrite, elemental sulfur, and sulfate. Fitting results for the deep sediment (>1 m) from Meander C also included mackinawite. Errors represent linear combination fitting model errors.

Sample	Pyrite, %	Elemental S, %	Sulfate, %	Mackinawite[a], %
Outcrop shale, bottom (0.8 m)	45 ± 3	34 ± 3	21 ± 0.4	--
Outcrop shale, middle (0.4 m)	54 ± 2	26 ± 2	20 ± 0.3	--
Outcrop shale, top (0 m)	11 ± 5	53 ± 5	36 ± 0.7	--
Hillslope shale, pristine (9 m)	69 ± 2	20 ± 2	11 ± 0.2	--
Hillslope shale, weathered (2.7 m)	50 ± 2	33 ± 2	17 ± 0.3	--
Meander C sediment (1.05-1.40 m)	6.8 ± 6.9	57 ± 6	33 ± 0.8	6.0 ± 1.6

[a] Mackinawite was only considered in the fit for Meander C.

3.2 Sulfur Speciation in Soil

Sulfur XANES spectra from hillslope soil samples are shown in Figures 2 and 4. In contrast with the shale samples, the hillslope soils show no clear evidence of reduced inorganic sulfur, suggesting that pyrite has been fully weathered/depleted from the solid phase in the soil zone that occurs in the top 1-m. Instead, hillslope soils have peaks in the 2472-2475 eV range (centered around 2473.4 eV), which coincide with those of the reduced organic sulfur compounds, represented by methionine, cystine, and cysteine, and a peak at 2475.5 eV which corresponds to sulfoxide (Prietzel et al., 2011). In addition, there is a significant peak at 2480.5 eV, which coincides with sulfonate compounds. The sulfonate peak occurs as a shoulder on the larger sulfate peak for the bulk soil samples. While none of the organic-S standards provided a precise fit to the observed spectra (Figure 4), the peaks at 2473.4 and 2480.5 eV can be assigned as reduced and oxidized organic sulfur, respectively. These organic-S peaks are commonly observed in bulk soil, soil organic matter (*e.g.*, humic and fulvic acids), and shale kerogen, although the relative proportion of reduced and oxidized organic sulfur is variable (Hutchison et al., 2001; Pomerantz et al., 2014; Prietzel et al., 2011; Prietzel et al., 2007; Wiltfong et al., 2005). Elemental sulfur and carbon depth profiles at the hillslope (Figure 2) are closely correlated in the top 2-m, with a C:S of approximately 60, providing further support for the predominance of organic-S in hillslope soil. Sulfur concentrations in soils are much lower (0.03-0.09%) compared to shale bedrock (0.6-2.5%) (Figure 2) and the incorporation of pyrite-derived sulfur into the organic soil cycle is likely limited by the seasonally-high water tables occurring during spring snowmelt, and the rooting depths of plants at the hillslope.

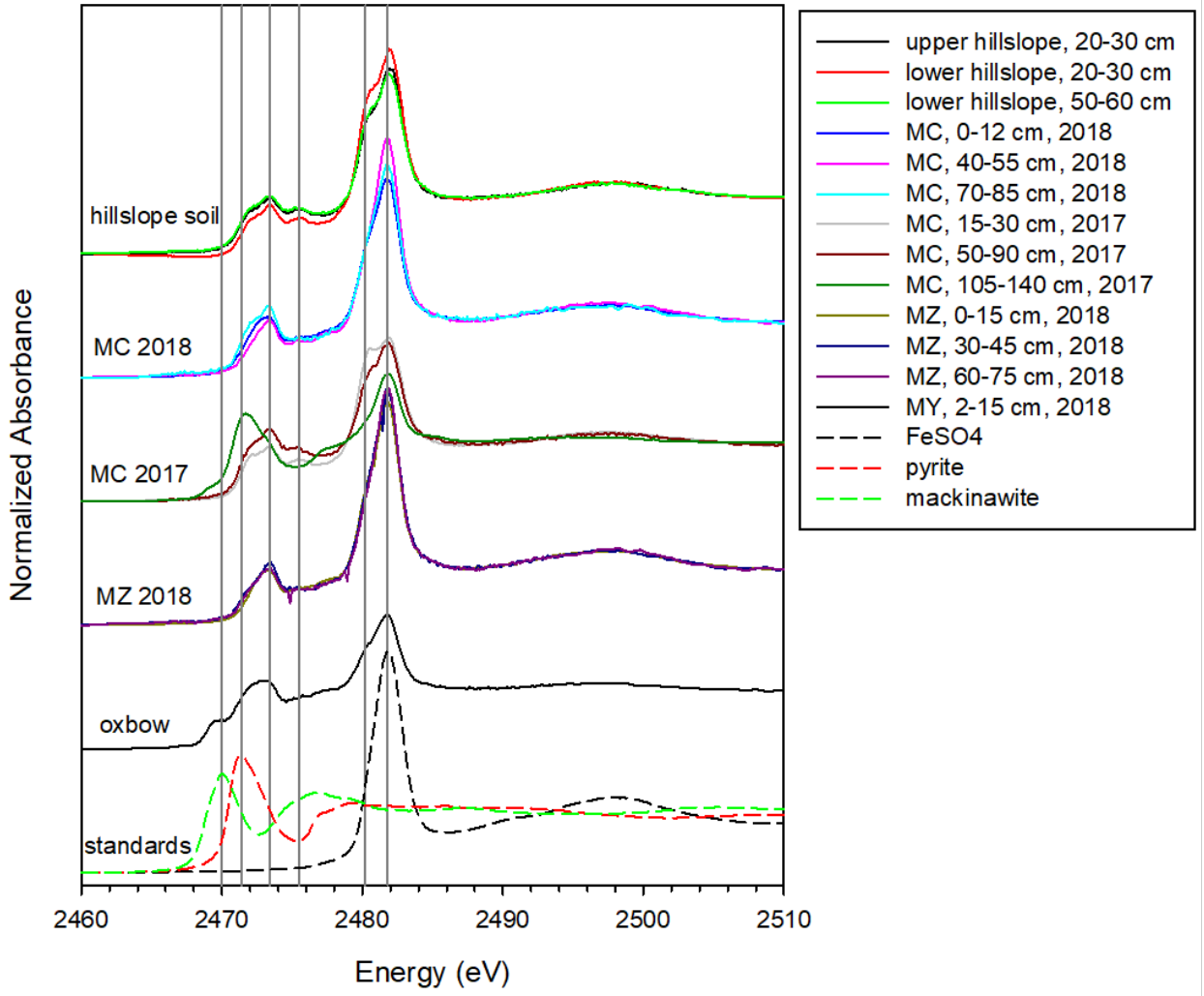

Figure 4. Sulfur K-edge XANES data from bulk hillslope soil and floodplain sediment from Meander C (MC), Meander Z (MZ) and Meander Y (MY, oxbow). Vertical lines indicate the locations of mackinawite, pyrite, reduced organic sulfur, sulfoxide, sulfonate, and sulfate peaks at 2470.0, 2471.4, 2473.4, 2475.5, 2480.2, and 2481.8 eV, respectively.

3.3 Sulfur Speciation in Floodplain Sediment

With the exception of the deepest Meander C sediment sample (105-140 cm), all floodplain sediment samples (Figure 4) had spectra which closely resembled that of the hillslope soil samples, with reduced organic-S, oxidized organic-S, and sulfate peaks at 2473.4, 2480.5, and 2481.8 eV, respectively. In the floodplain, alluvial sediment, including both shale and non-shale materials, is deposited by the river on top of weathered shale bedrock. However, over time, continued rock weathering and soil development processes (*e.g.*, plant growth and root-driven processes) can also occur in the floodplain.

373 The similarity between the shallow hillslope soil and shallow floodplain sediment spectra suggest that
374 sulfur processing is similar in these two unsaturated (or seasonally saturated) environments.

375 Only two sediment samples (Meander C, 105-140 cm 2017 and Meander Y, 2-15 cm) showed
376 clear evidence of inorganic sulfide phases. The Meander C 105-140 cm sediment sample had a spectrum
377 which closely resembled that of weathered shale, with peaks at 2471.4 and 2481.8 eV, representing
378 reduced inorganic sulfur and sulfate, respectively. This sample is from the deepest location in the
379 floodplain and may indeed be intercepting the weathered shale located beneath the alluvium or may
380 represent transported (alluvial) shale. This zone (>1 m) also remains saturated year-round and thus may
381 be subjected to minimal oxidation. Sediment samples collected from Meander C in 2018 only reached 85
382 cm bgs, and thus did not intercept the permanently-saturated weathered shale layer. The sample
383 collected from Meander Y is located in the former river bed of a cut-off meander (oxbow) and was
384 saturated when the sample was collected, as it is for much of the year. While this sample did not have a
385 clear pyrite peak, there was a peak at 2470 eV consistent with mackinawite. Mackinawite was not
386 observed in the hillslope or outcrop shale samples (Figure 2), therefore, it is likely formed as a secondary
387 product of sulfur reduction in the anoxic environment of the oxbow. A small mackinawite peak is also
388 present in the deepest Meander C sample (105-140 cm), again presumably formed as a secondary
389 mineral within the saturated floodplain environment. Linear combination fitting of the Meander C 105-
390 140 cm spectra revealed 6.8% pyrite, 57% elemental S, 33% sulfate, and 6% mackinawite as shown in
391 Table 1. This sample had less pyrite and more elemental sulfur than any of the other shale samples
392 analyzed, suggesting it is even more highly weathered than the exposed shale outcrop (Outcrop top).
393 Mackinawite, FeS, can be produced during dissimilatory sulfate reduction; however, it is considered to
394 be metastable and may be a precursor to the more thermodynamically stable pyrite (FeS_2) (Rickard and
395 Luther, 2007).

396 The Meander C 105-140 cm floodplain sample may also have some reduced organic S, as
397 evidenced by the shoulder at 2473.4 eV which is not fully captured by fitting with inorganic S standards
398 alone (Figure S2). This organic-S signal may result from either residual shale-kerogen or relatively fresh
399 microbial and plant-derived organic sulfur. Radiocarbon measurements demonstrated that shale-
400 derived organic carbon made up a significant portion of the total organic carbon in East River floodplain
401 sediments, with greater proportions of shale-derived OC present at depth and in active depositional
402 environments within the floodplain (Fox et al., 2020). This suggests that shale kerogen may be
403 responsible for some of the observed organic-S in the mineral fraction. Organic-S was also observed in

μ-XANES spectra from a pyrite-depleted zone in the weathered shale, but not in bulk shale spectra, likely because the kerogen-S content is expected to be much lower than the inorganic sulfur content and therefore may be difficult to detect in the more pristine, unweathered shale samples.

3.4 Sulfur Speciation in Density Fractions

Soil and sediment samples subjected to density fractionations revealed small differences between the sulfur spectra of bulk, light, and heavy fractions, representing bulk soil or sediment, plant litter, and mineral pools, respectively (Figure 5 and Figure S3). Notably, the sulfate peak (2481.8 eV) is much lower in both the heavy and light density fractions compared to the bulk. This is likely due to dissolution and loss of highly soluble sulfate minerals or precipitates during the density fractionation procedure. Note that inorganic and organic sulfates (*i.e.*, ester sulfate) are very difficult to distinguish by K-edge XANES due to their close peak energies (Prietzel et al., 2007), and much of the intensity at 2481.8 eV in the light fractions is likely due to organic sulfates. The similarity in intensity for the sulfonate (2480.2 eV) and sulfate (2481.8 eV) peaks in the light fractions suggests similar concentrations of organic sulfates and sulfonates in these samples. As with the bulk sample, the heavy fraction from the deepest Meander C sample (105-140 cm) closely resembled the spectra of weathered shale, but with a smaller sulfate peak. However, the light fraction from the same sample appeared to be very similar to the other light fraction samples. Both the heavy and light fractions have large organic sulfur peaks at 2473.4 eV (reduced organic sulfur) and 2480.2 eV (sulfonate). However, in the heavy fractions, the peak centered at 2473.4 eV is a bit broader, with greater intensity around 2472 eV, compared to the light fractions. This suggests the presence of a small fraction of reduced inorganic sulfur (elemental sulfur or sulfide) present in the mineral fraction of all three heavy fractions.

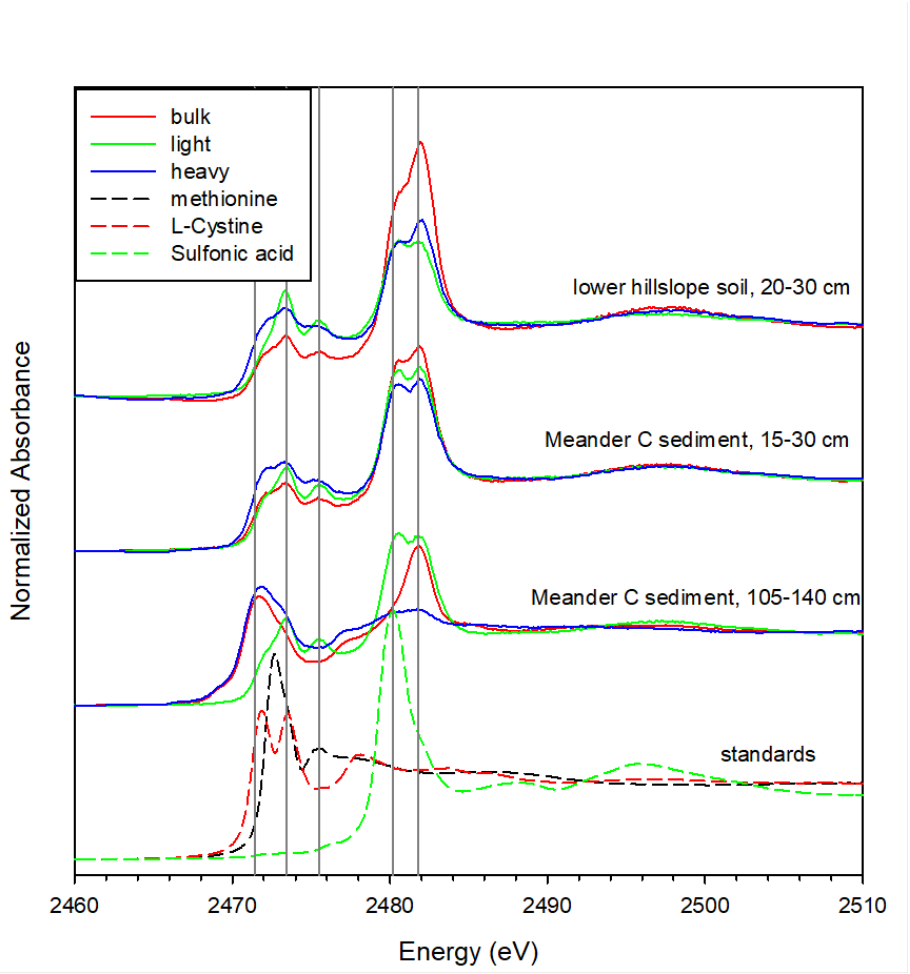

Figure 5. Comparison of density fractions for soil and sediment samples. Vertical lines indicate the locations of pyrite, organic sulfide, sulfoxide, sulfonate, and sulfate peaks at 2471.4, 2473.4, 2475.5, 2480.2, and 2481.8 eV, respectively. Standards representing reduced organic S (methionine and L-cystine) and sulfonic acid (taurine) are also shown.

3.5 Impact of Hydrology on Sulfur Speciation in Soil and Sediment

A comparison of bulk soil and shallow (<1 m) floodplain sediment spectra reveal small differences among samples, primarily in the intensity of the sulfate peak, with no clear trends with depth or across locations. For example, hillslope soils are very similar to the Meander C sediments collected in June 2017 (Figure 4). Similarly, sediment samples collected from two different meanders in June-July 2018 are also very similar to one another. However, the sediment samples collected in 2018 all have much larger sulfate peaks compared to soil and sediment collected in 2017. While there were some slight differences in the sediment processing and analysis procedures at these two dates, there were also large differences in the environmental conditions at the time of sampling. 2017 was a very large snowpack year, with corresponding high river discharge and groundwater levels, whereas 2018

441 was a drought year, with low river discharge and groundwater levels (Figure 6). 2017 samples were
442 collected close to peak river discharge when floodplain sediment samples were completely saturated,
443 whereas 2018 samples were collected when groundwater levels were approximately 0.8 m below
444 ground surface, and thus sediments were unsaturated. Due to the high solubility of sulfate minerals, we
445 expect a large portion of the inorganic sulfate to be leached from shallow sediments during high
446 discharge periods when sediments are completely saturated, and accumulate in the unsaturated zone
447 sediments when water levels are lower. We also note that organic sulfates may be responsible for a
448 significant portion of the sulfate signal, and are less likely to leached from sediments under saturated
449 conditions. This suggests that inorganic sulfate contents may be highly dependent on the saturation
450 state of the sediments, while organic sulfate content is not.

451 Dissolved sulfate concentrations in shallow groundwater (1-1.5 m bgs) and river water are
452 shown in Figure 6B. The shallow groundwater exhibits a dip in sulfate concentrations that occurs 1-2
453 months after the dip in sulfate concentration in the river which occurs at peak discharge. River water is
454 transported laterally across the meanders (lateral hyporheic exchange) with modeled water transport
455 times of 1-2 months across Meander C (Dwivedi et al., 2018). The dip in sulfate concentrations in the
456 groundwater thus reflects this lateral transport from the river through the intra-meander zone.
457 However, the transport of sulfate through the meanders does not appear to be completely conservative.
458 In 2017, when river discharge was very high, dissolved sulfate concentrations in Meander C were higher
459 than river water concentrations, suggesting flushing of sulfate from shallow floodplain sediments. A
460 similar flushing behavior seems to occur in Meander Z in 2018. However, Meander C porewater
461 concentrations are much lower in 2018, and late in the season in 2017, suggesting that deeper,
462 permanently saturated sediments may serve as a sink for sulfate when river discharge is lower. This
463 observation is consistent with those of Dwivedi et al. (2018), who noted that the groundwater velocities
464 across Meander C were lowest during periods of low discharge. Slower groundwater velocities promote
465 reducing conditions because biological consumption outpaces transport of dissolved oxygen across the
466 meander. This implies active sulfur cycling in floodplain sediments that is closely linked to the
467 hydrological conditions, and the floodplain sediments may alternate between being a source or sink for
468 sulfur on a seasonal time period.

469

470

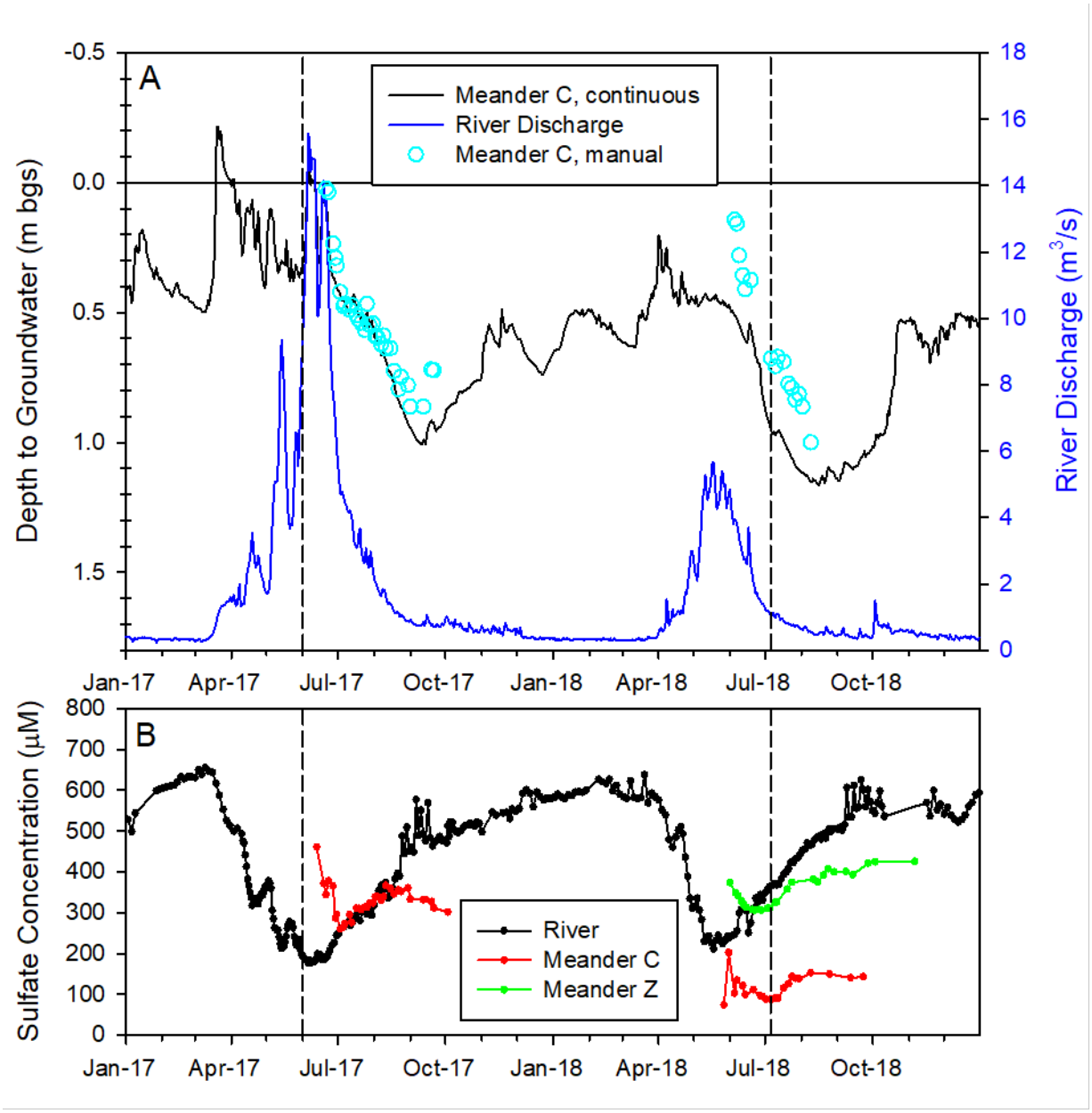

Figure 6. (A) East River discharge at the pumphouse and groundwater levels from manual measurements at the sediment sampling location (Meander C) and continuous monitoring at a nearby well (CPA3). (B) Dissolved sulfate concentrations in the river water (pumphouse) and groundwater (Meander C, Meander Z). Dashed lines indicate the sediment sampling times. Groundwater elevation data for CPA3 from (Dafflon et al., 2020), river discharge from (Carroll and Williams, 2019), river SO4 data from (Williams et al., 2020), and groundwater sulfate data from Fox et al., 2021a, 2021b, 2021c.

3.6 Sulfate Reduction in the Floodplain: Aqueous Geochemical Evidence

Figure 7 shows measurements of dissolved organic carbon (DOC), Fe, and sulfate from 2018 in >1-m deep piezometers along transects across Meander C and Meander Z. While direct measurement of

solid-phase S speciation can only be performed on a limited number of samples, more routine aqueous chemistry measurements of water samples can provide indirect evidence of sulfate reduction. Meander C exhibits anoxic conditions in the saturated zone, with low (-50 to -200 mV) redox potentials (Figure S4), dissolved Fe and DOC concentrations much higher than river water concentrations, and dissolved sulfate concentrations lower than river water concentrations in both July and September. By contrast, Meander Z exhibits oxic conditions in the saturated zone, with high (13 to 200 mV) redox potentials (Figure S4) and low dissolved Fe and DOC concentrations that are similar to river water. In July, sulfate concentrations increase along the transect at Meander Z, reaching concentrations that are higher than river water concentrations. This may reflect flushing of sulfate accumulated in the shallow (<1 m), seasonally saturated zone. However, in September, sulfate concentrations are flat across Meander Z and slightly lower than river water concentrations, possibly due to sulfate reduction. Reducing conditions are more likely to occur during periods of low discharge when groundwater velocities are lower (Dwivedi et al., 2018). This suggests that the Meander Z sediments may serve as a source of sulfate to the river during snowmelt when water levels are high, and may transition to a sink for sulfate during baseflow. The finer-grained and thus lower permeability sediments of Meander C provide the conditions necessary for sulfate reduction to occur, while the coarser-grained, higher-permeability sediments of Meander Z remain oxic for much of the year. Sulfate reduction rates tend to be highest in anoxic zones that are rich in organic carbon and have high inputs of dissolved sulfate (Holmer and Storkholm, 2001; Ng et al., 2017; Pester et al., 2012). While traditionally the concept of the redox ladder has suggested that sulfate reduction will only proceed after iron reduction has depleted the pool of ‘available’ Fe(III), recent work has shown that sulfate reduction can proceed concurrently with Fe reduction (Hansel et al., 2015).

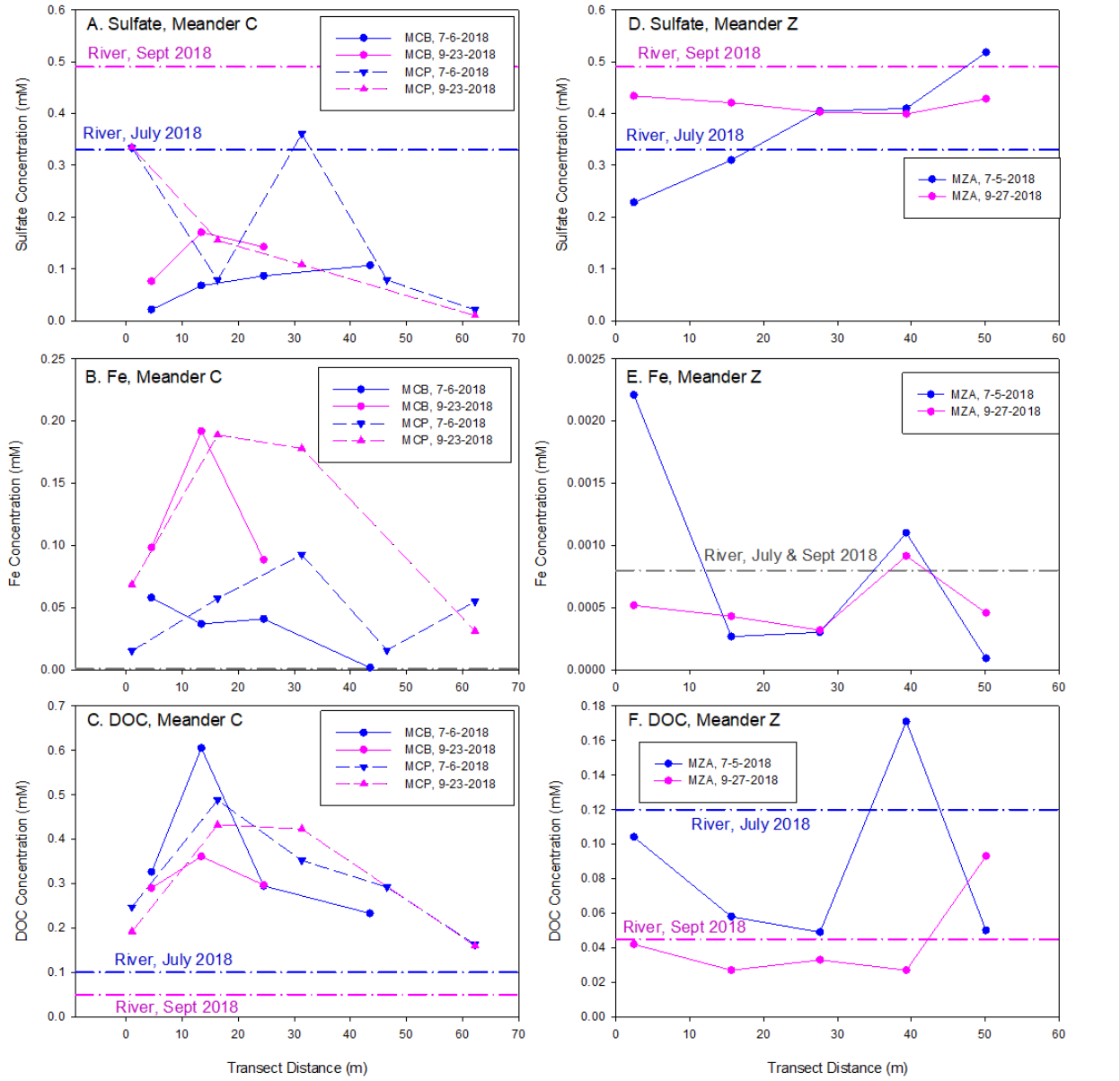

Figure 7. Comparison of dissolved sulfate, dissolved Fe, and dissolved organic carbon (DOC) concentrations in shallow piezometers along transects across Meander C (A-C) and Meander Z (D-F) in July and September 2018. Note the different concentration scales between Meanders C and Z. Data is shown for two transects across Meander C (MCB and MCP) and one transect across Meander Z (MZA). River water concentrations are shown as horizontal dashed lines. Data from Fox et al., 2021a; 2021b.

Figure 8 shows sulfate concentrations and sulfate sulfur isotope ratios from groundwater samples collected from piezometers across Meanders C and D compared to river water values. Beginning about 16 m from the river, there is a clear trend of decreasing sulfate concentrations and a

corresponding increase in $\delta^{34}S$, which is indicative of biological sulfate reduction. The dashed line plotted on Figure 8 reflects this trend of no sulfate reduction for the first 16 m into the meanders followed by a simple linear sulfate reduction trend of 7.5 μM/meter. These concentrations were used to calculate the Rayleigh isotope fractionation trend for the sulfate as it moves through the meander under sulfate reducing conditions. The fractionation factor, α, used for these calculations was 1.030, which is typical for biological sulfate reduction (Canfield, 2018). Dissolved sulfate concentrations in the river, and to a lesser extent in the meander groundwater, vary seasonally with snowmelt and river discharge (Figure 6), due primarily to mixing of snowmelt and deeper groundwater and hyporheic transport from river across meanders. Mixing of groundwaters with differing concentrations of sulfate may also be partially responsible for the variability in sulfate concentrations in meander groundwater. However, none of these processes would produce the isotopic trends observed in these two meanders, especially given that the meanders are on opposite sides of the river. Loss of sulfate in the meander groundwater through sulfate reduction is clearly an important factor in removing sulfate from the East River system in these organic-rich intra-meander zones.

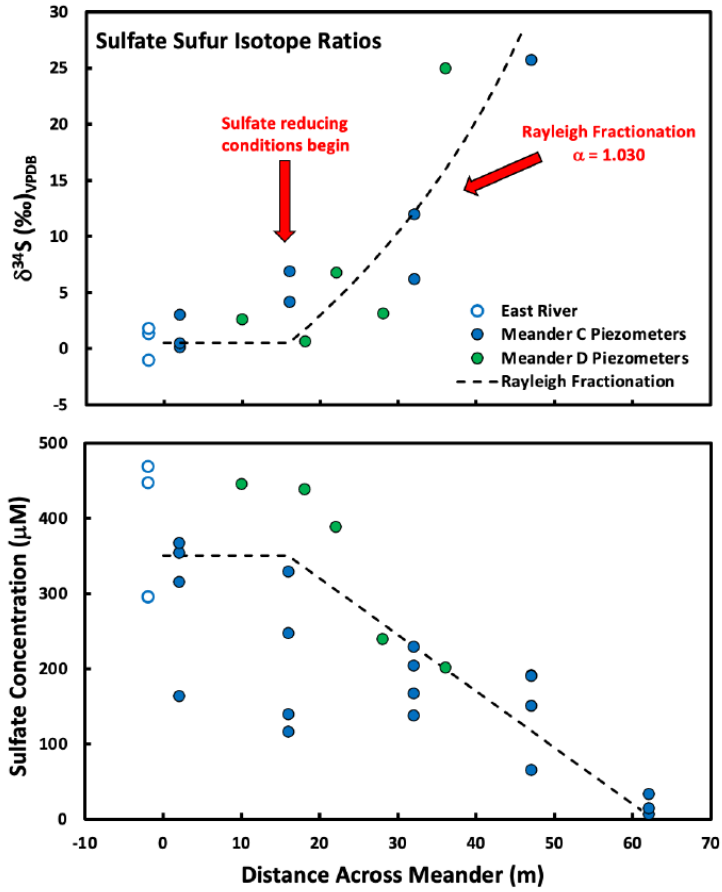

Figure 8. Dissolved sulfate and sulfate $\delta^{34}S$ in shallow piezometers along transects across Meander C and Meander D between July 2015 and September 2016. River water values are also shown. The Rayleigh isotope fractionation trend is shown with a dashed line. Note that sulfate concentrations in the piezometer at 62-m were too low for $\delta^{34}S$ determination.

4. Conclusions

Through the use of a combination of sulfur XANES analysis and aqueous geochemical measurements, we have gained insight into the biogeochemical cycling of sulfur in a pristine, high elevation watershed. Figure 9 shows a conceptual diagram of sulfur cycling which highlights the key processes affecting sulfur speciation, transformation, and transport in such a system. Pyrite from shale bedrock serves as the primary source of sulfur in this system, and sulfur XANES analysis of shale samples revealed clear evidence of pyrite oxidation to sulfate in shale weathering profiles, with significant accumulations (20-53%) of elemental sulfur intermediate. Although elemental sulfur has been proposed as an intermediate in the pyrite oxidation pathway (Nordstrom, 2000), it is often missed in shale weathering studies due to the insensitivity of bulk analytical techniques (*e.g.*, XRD) to this form of sulfur.

However, our results demonstrate that elemental sulfur is a major form of sulfur in partially weathered shale. Pyrite weathering from shale bedrock is often assumed to be a unidirectional process; however, our micro-scale data reveals dynamic sulfur cycling occurring near fracture surfaces in the weathered shale, including the accumulation of sulfur as pyrite at fracture surfaces within the permanently saturated zone at the toeslope, where sulfur concentrations reach five times the concentrations in underlying unfractured bedrock. Whether this narrow zone of pyrite accumulation serves as a source or sink for sulfur in future climate scenarios depends on the degree to which water tables drop in this zone; if water tables drop below the accumulation zone, the accumulated pyrite will be exposed and subject to oxidation. Weathered shale underlying floodplain sediments (1.0-1.4 m bgs) which remains saturated year-round, had very little (<10%) pyrite remaining, but had a large pool of elemental S (57 ± 6%). The resulting concentrations of pyrite in these samples, particularly in highly weathered shale samples, may be too low to detect using conventional X-ray diffraction (XRD). However, due to the presence of elemental S, reduced inorganic S still makes up the majority of the solid-phase S in these deep floodplain and highly weathered shale bedrock zones and may serve as a continued source of dissolved sulfate if these samples are exposed to oxidizing conditions.

Sulfate released from shale weathering is highly soluble and can be transported away from shale bedrock, retained on soil exchange sites, and taken up by plants and microbes and converted to organic-S. Our data shows a near complete loss of reduced inorganic sulfur and conversion to an organic-S dominated system occurring in the top meter of both hillslope soils and floodplain sediments. Sulfur concentrations in soils are 10-20 times lower than in shale bedrock, suggesting that soils serve as a limited sink for shale-derived sulfur. The sulfur retained by hillslope soils is almost completely integrated into the plant and microbially driven organic cycling processes of active soils, as it is in most upland soils (Prietzel et al., 2011; Prietzel et al., 2007; Wilhelm Scherer, 2009). The presence of an active sulfur cycle was observed in the microbial data by Matheus Carnevali et al. (2021) who showed that genes encoding for S oxidation, including sulfide, sulfite, and thiosulfate oxidation, are prevalent in shallow floodplain soils (10-25 cm bgs) in the East River. Lavy et al. (2019) observed that saturated floodplain sediments in the East River supported an anaerobic microbial community, with a greater abundance of genes encoding for anaerobic carbon and nitrogen fixation and sulfur reduction, which was distinct from that in shallower unsaturated floodplain sediments and hillslope soils. Higher amounts of litter-derived organic matter and more oxic conditions in these shallow soil zones promote the biogeochemical cycling of sulfur, which is intricately linked with other nutrient cycles (*e.g.*, carbon and nitrogen), through plant uptake, litter deposition and decomposition, and microbial processing.

575 Nutrient-rich anoxic zones, which are abundant in the river corridor, can promote sulfate
576 reduction to sulfide, as evidenced by the observation of mackinawite formation in saturated oxbow
577 sediments and in weathered shale underlying floodplain sediments (1.0-1.4 m bgs). Aqueous sulfate
578 isotopic measurements provided additional evidence for active sulfate reduction along transects across
579 two meanders in the floodplain. Somewhat counter-intuitively, sulfate-reducing zones in the floodplain
580 may actually become more prevalent as water levels decline. Lower river discharge results in slower
581 groundwater velocities across the meanders (Dwivedi et al., 2018), promoting reducing conditions.
582 Other areas of the floodplain may also have conditions ideal for sulfate reduction. For example,
583 numerous off-channel oxbows and beaver ponds can be found in the floodplain; Briggs et al. (2019)
584 demonstrated that subsurface return flows (seepage zones) from beaver ponds in the East River were
585 chemically reduced, with elevated dissolved Fe (and other metal ion) concentrations and low oxidation-
586 reduction potential (ORP). Beaver dam-building occurs during periods of low river discharge, and river
587 water depth is one of the key factors influencing beaver dam building (Swinnen et al., 2019; Westbrook
588 et al., 2006), suggesting that the number of beaver ponds may increase with dropping water levels. We
589 hypothesize that these wetlands may serve as a major sink for sulfur in the river corridor, attenuating
590 the flux of sulfate in the river.

591 As climate changes we may expect oxidative weathering of shale-pyrite to increase due to falling
592 water tables, lower snowpack, and other hydrologic changes (Manning et al., 2013; Mast et al., 2011;
593 Rogora et al., 2003; Sommaruga-Wögrath et al., 1997; Wögrath and Psenner, 1995). However, the
594 export of sulfate from the watershed is ultimately controlled by the coupling of sulfur cycles between
595 different watershed compartments, such as soils, groundwater, and the river corridor. Our results show
596 that individual watershed compartments show distinct sulfur cycling which may respond differently to
597 climate change. While plant/microbial uptake and transformation to organic-S in shallow soils and
598 sediments may serve as a limited sink for newly released sulfur, the reduction of sulfate to sulfide in
599 anoxic hyporheic-zone sediments is a significant sulfur sink and may in fact increase with climate
600 change, partially offsetting the increased released of dissolved sulfate from pyrite weathering. The
601 deeper understanding of sulfur cycles in these inter-connected watershed compartments will allow us to
602 make better predictions of the whole watershed response to climate change.

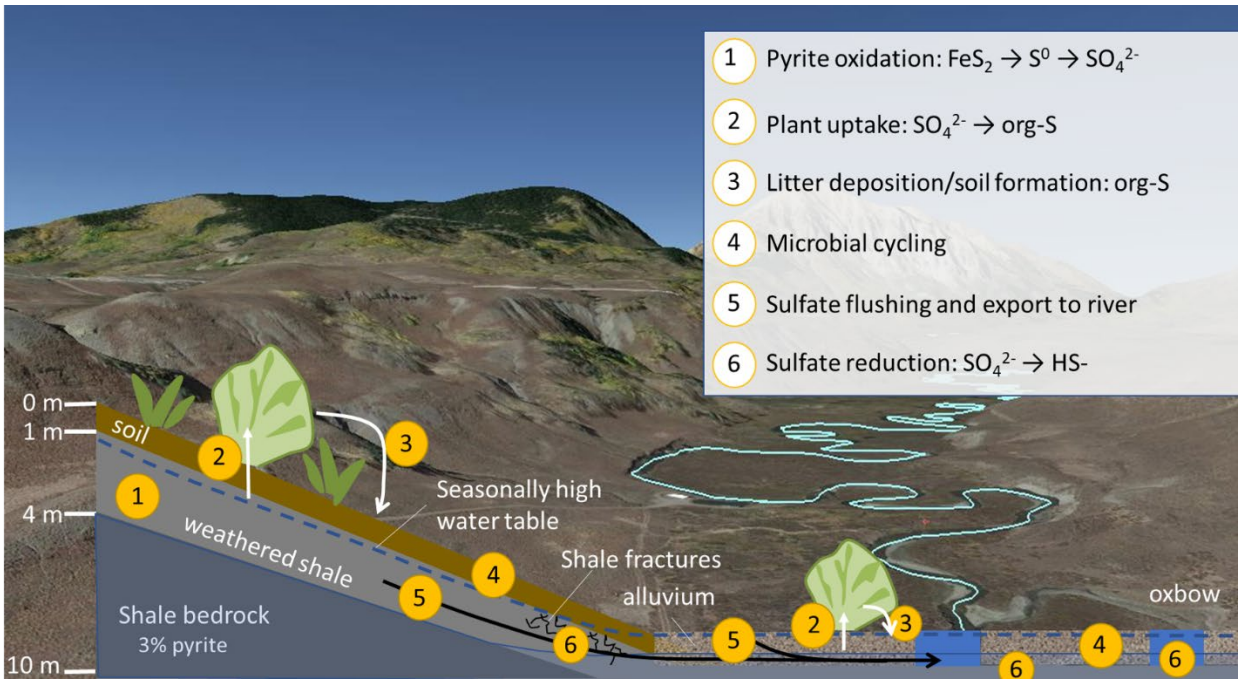

Figure 9. Conceptual diagram showing sulfur cycling in the East River watershed.

Acknowledgements, Samples and Data

This work was supported by the Watershed Function Scientific Focus Area funded by the U.S. Department of Energy, Office of Science, Office of Biological and Environmental Research under contract number DE-AC02-05CH11231 with Lawrence Berkeley National Laboratory. C.A., C.D., M.K., H.N., and S.F. were supported by the Department of Energy, Office of Biological and Environmental Research, Subsurface Biosphere Research program (award no. DE-SC0016544). Work by K.B. was supported by the Floodplain Hydro-Biogeochemistry Science Focus Area funded by the U.S. Department of Energy office of Biological and Environmental Research, under contract number DE- AC02-76SF00515 with SLAC.

This research used resources of the Advanced Light Source, a U.S. DOE Office of Science User Facility under contract no. DE-AC02-05CH11231. Portions of research described in this paper was performed at the Canadian Light Source, which is supported by the Canada Foundation for Innovation, Natural Sciences and Engineering Research Council of Canada, the University of Saskatchewan, the Government of Saskatchewan, Western Economic Diversification Canada, the National Research Council Canada, and the Canadian Institutes of Health Research. Use of the Stanford Synchrotron Radiation Lightsource, SLAC National Accelerator Laboratory, is supported by the U.S. Department of Energy, Office of Science, Office of Basic Energy Sciences under Contract No. DE-AC02-76SF00515. The SSRL Structural Molecular Biology Program is supported by the DOE Office of Biological and Environmental

Research, and by the National Institutes of Health, National Institute of General Medical Sciences (P30GM133894). The contents of this publication are solely the responsibility of the authors and do not necessarily represent the official views of NIGMS or NIH.

The data used in this work is available online at the ESS-DIVE database (Fox et al., 2022).

Supporting Information

Supporting information (SI) includes figures showing linear combination fits of shale sulfur XANES spectra and supplemental sulfur XANES spectra for density fractions of soils and sediments. In addition, tables showing solid-phase and groundwater sampling locations and shale spectra linear combination fitting results with and without elemental sulfur are shown in the SI. This data is available online free of charge.

References

Briggs, M. A., Wang, C., Day-Lewis, F. D., Williams, K. H., Dong, W., & Lane, J. W. (2019). Return flows from beaver ponds enhance floodplain-to-river metals exchange in alluvial mountain catchments. *Science of the Total Environment, 685*, 357-369. https://doi.org/10.1016/j.scitotenv.2019.05.371

Canfield, D. E. (2018). Biogeochemistry of Sulfur Isotopes. In J. W. Valley & D. R. Cole (Eds.), *Stable isotope geochemistry* (Vol. 43, pp. 607-636).

Carroll, R., & Williams, K. H. (2019). [Dataset] Discharge data collected within the East River for the Lawrence Berkeley National Laboratory Watershed Function Science Focus Area (water years 2015-2018), Watershed Function SFA, ESS-DIVE repository. doi:10.21952/WTR/1495380

Carroll, R. W. H., Bearup, L. A., Brown, W., Dong, W., Bill, M., & Willlams, K. H. (2018). Factors controlling seasonal groundwater and solute flux from snow-dominated basins. *Hydrological Processes, 32*(14), 2187-2202. https://doi.org/10.1002/hyp.13151

Dafflon, B., Malenda, H., & Dwivedi, D. (2020). [Dataset] Groundwater level elevation and temperature across Meander C at the Lower Montane in the East River Watershed, Colorado. Watershed Function SFA, ESS-DIVE repository. doi:10.15485/1647041

Dwivedi, D., Steefel, C. I., Arora, B., Newcomer, M., Moulton, J. D., Dafflon, B., et al. (2018). Geochemical Exports to River From the Intrameander Hyporheic Zone Under Transient Hydrologic Conditions: East River Mountainous Watershed, Colorado. *Water Resources Research, 54*(10), 8456-8477. doi:10.1029/2018WR023377

Falco, N., Wainwright, H., Dafflon, B., Léger, E., Peterson, J., Steltzer, H., et al. (2019). Investigating microtopographic and soil controls on a mountainous meadow plant community using high-resolution remote sensing and surface geophysical data. *Journal of Geophysical Research: Biogeosciences, 124*, 1618–1636. https://doi.org/10.1029/2018JG004394

Fleet, M. E. (2005). XANES spectroscopy of sulfur in earth materials. *The Canadian Mineralogist, 43*(6), 1811-1838.

Fox, P. M., Anderson, C., Dewey, C., Keiluweit, M., & Nico, P. S. (2021a). [Dataset] 2017 Meander C and O floodplain groundwater chemistry from the East River, Colorado. Watershed Function SFA, ESS-DIVE repository. doi:10.15485/1835881

Fox, P.M., Dewey, C., Anderson, C., Keiluweit, M., Nico, P.S. (2021b). [Dataset] 2018 Meander Y and Meander Z floodplain groundwater chemistry from the East River watershed, Colorado. Watershed Function SFA, ESS-DIVE repository. doi:10.15485/1838122

Fox, P.M., Anderson, C., Keiluweit, M., Dewey, C., Nico, P.S. (2021c). [Dataset] 2018 Meander C floodplain groundwater chemistry from the East River watershed, Colorado. Watershed Function SFA, ESS-DIVE repository. doi:10.15485/1836833

Fox, P.M., Anderson, C., Dewey, C., Keiluweit, M., Naughton, H.R., Fendorf, S., Nico, P.S. (2022). [Dataset] Sulfur x-ray absorption spectroscopy data from bedrock shale, soil, and floodplain sediment from the East River, Colorado watershed. Watershed Function SFA, ESS-DIVE repository. doi:10.15485/1860454

Gaskill, D. L., Mutschler, F. E., Kramer, J. H., Thomas, J. A., & Zahony, S. G. (Cartographer). (1991). Geologic map of the Gothic quadrangle, Gunnison County, Colorado [Report]. Retrieved from http://pubs.er.usgs.gov/publication/gq1689

Hansel, C. M., Lentini, C. J., Tang, Y., Johnston, D. T., Wankel, S. D., & Jardine, P. M. (2015). Dominance of sulfur-fueled iron oxide reduction in low-sulfate freshwater sediments. *The ISME Journal, 9*(11), 2400-2412. https://doi.org/10.1038/ismej.2015.50

Herlihy, A. T., & Mills, A. L. (1985). Sulfate Reduction in Freshwater Sediments Receiving Acid Mine Drainage. *Applied and Environmental Microbiology, 49*(1), 179-186. doi:10.1128/aem.49.1.179-186.1985

Holmer, M., & Storkholm, P. (2001). Sulphate reduction and sulphur cycling in lake sediments: a review. *Freshwater Biology, 46*(4), 431-451. https://doi.org/10.1046/j.1365-2427.2001.00687.x

Hutchison, K. J., Hesterberg, D., & Chou, J. W. (2001). Stability of Reduced Organic Sulfur in Humic Acid as Affected by Aeration and pH. *Soil Science Society of America Journal, 65*(3), 704-709. https://doi.org/10.2136/sssaj2001.653704x

Lami, A., Marchetto, A., Musazzi, S., Salerno, F., Tartari, G., Guilizzoni, P., et al. (2010). Chemical and biological response of two small lakes in the Khumbu Valley, Himalayas (Nepal) to short-term variability and climatic change as detected by long-term monitoring and paleolimnological methods. *Hydrobiologia, 648*(1), 189-205. https://doi.org/10.1007/s10750-010-0262-3

Lavy, A., McGrath, D. G., Matheus Carnevali, P. B., Wan, J., Dong, W., Tokunaga, T. K., et al. (2019). Microbial communities across a hillslope-riparian transect shaped by proximity to the stream, groundwater table, and weathered bedrock. *Ecology and Evolution, 9*(12), 6869-6900. https://doi.org/10.1002/ece3.5254

Manning, A. H., Verplanck, P. L., Caine, J. S., & Todd, A. S. (2013). Links between climate change, water-table depth, and water chemistry in a mineralized mountain watershed. *Applied Geochemistry, 37*, 64-78. https://doi.org/10.1016/j.apgeochem.2013.07.002

Mast, M. A., Turk, J. T., Clow, D. W., & Campbell, D. H. (2011). Response of lake chemistry to changes in atmospheric deposition and climate in three high-elevation wilderness areas of Colorado. *Biogeochemistry, 103*(1), 27-43. https://doi.org/10.1007/s10533-010-9443-4

Matheus Carnevali, P. B., Lavy, A., Thomas, A. D., Crits-Christoph, A., Diamond, S., Méheust, R., et al. (2021). Meanders as a scaling motif for understanding of floodplain soil microbiome and biogeochemical potential at the watershed scale. *Microbiome, 9*(1), 121. https://doi.org/10.1186/s40168-020-00957-z

Mermut, A. R., & Arshad, M. A. (1987). Significance of Sulfide Oxidation in Soil Salinization in Southeastern Saskatchewan, Canada. *Soil Science Society of America Journal, 51*(1), 247-251. https://doi.org/10.2136/sssaj1987.03615995005100010050x.

Mikutta, R., Schaumann, G. E., Gildemeister, D., Bonneville, S., Kramer, M. G., Chorover, J., et al. (2009). Biogeochemistry of mineral–organic associations across a long-term mineralogical soil gradient (0.3–4100kyr), Hawaiian Islands. *Geochimica et Cosmochimica Acta, 73*(7), 2034-2060. https://doi.org/10.1016/j.gca.2008.12.028

Morrison, S. J., Goodknight, C. S., Tigar, A. D., Bush, R. P., & Gil, A. (2012). Naturally Occurring Contamination in the Mancos Shale. *Environmental Science & Technology, 46*(3), 1379-1387. http://dx.doi.org/10.1021/es203211z

Nettleton, W. D., Nelson, R. E., Brasher, B. R., & Derr, P. S. (1982). Gypsiferous Soils in the Western United States. In *Acid Sulfate Weathering* (pp. 147-168). https://doi.org/10.2136/sssaspecpub10.c9

Ng, G.-H. C., Yourd, A. R., Johnson, N. W., & Myrbo, A. E. (2017). Modeling hydrologic controls on sulfur processes in sulfate-impacted wetland and stream sediments. *Journal of Geophysical Research: Biogeosciences, 122*(9), 2435-2457. https://doi.org/10.1002/2017JG003822

Nordstrom, D. K. (2000). Advances in the Hydrogeochemistry and Microbiology of Acid Mine Waters. *International Geology Review, 42*(6), 499-515. https://doi.org/10.1080/00206810009465095

Nordstrom, D. K. (2009). Acid rock drainage and climate change. *Journal of Geochemical Exploration, 100*(2), 97-104. https://doi.org/10.1016/j.gexplo.2008.08.002

Nordstrom, D. K. (2011). Hydrogeochemical processes governing the origin, transport and fate of major and trace elements from mine wastes and mineralized rock to surface waters. *Applied Geochemistry, 26*(11), 1777-1791. https://doi.org/10.1016/j.apgeochem.2011.06.002

Pester, M., Knorr, K.-H., Friedrich, M., Wagner, M., & Loy, A. (2012). Sulfate-reducing microorganisms in wetlands – fameless actors in carbon cycling and climate change. *Frontiers in Microbiology, 3*(72). Review. Doi: 10.3389/fmicb.2012.00072

Pomerantz, A. E., Bake, K. D., Craddock, P. R., Kurzenhauser, K. W., Kodalen, B. G., Mitra-Kirtley, S., & Bolin, T. B. (2014). Sulfur speciation in kerogen and bitumen from gas and oil shales. *Organic Geochemistry, 68*, 5-12. https://doi.org/10.1016/j.orggeochem.2013.12.011

Prietzel, J., Botzaki, A., Tyufekchieva, N., Brettholle, M., Thieme, J., & Klysubun, W. (2011). Sulfur Speciation in Soil by S K-Edge XANES Spectroscopy: Comparison of Spectral Deconvolution and Linear Combination Fitting. *Environmental Science & Technology, 45*(7), 2878-2886. https://doi.org/10.1021/es102180a

Prietzel, J., Thieme, J., Salomé, M., & Knicker, H. (2007). Sulfur K-edge XANES spectroscopy reveals differences in sulfur speciation of bulk soils, humic acid, fulvic acid, and particle size separates. *Soil Biology and Biochemistry, 39*(4), 877-890. https://doi.org/10.1016/j.soilbio.2006.10.007

Ravel, B., & Newville, M. (2005). ATHENA, ARTEMIS, HEPHAESTUS: data analysis for X-ray absorption spectroscopy using IFEFFIT. *Journal of synchrotron radiation, 12*(4), 537-541.

Rickard, D., & Luther, G. W. (2007). Chemistry of Iron Sulfides. *Chemical Reviews, 107*(2), 514-562. https://doi.org/10.1021/cr0503658

Rickard, D., & Morse, J. W. (2005). Acid volatile sulfide (AVS). *Marine Chemistry, 97*(3), 141-197. https://doi.org/10.1016/j.marchem.2005.08.004

Rogora, M., Mosello, R., & Arisci, S. (2003). The effect of climate warming on the hydrochemistry of Alpine lakes. *Water, Air, and Soil Pollution, 148*(1-4), 347-361. Doi: 10.1023/A:1025489215491

Singer, D. M., Herndon, E., Cole, K., Burkey, M., Morisson, S., Cahill, M., & Bartucci, M. A. (2020). Micron-scale distribution controls metal(loid) release during simulated weathering of a Pennsylvanian coal shale. *Geochimica et Cosmochimica Acta, 269*, 117-135. https://doi.org/10.1016/j.gca.2019.10.034

Sommaruga-Wögrath, S., Koinig, K. A., Schmidt, R., Sommaruga, R., Tessadri, R., & Psenner, R. (1997). Temperature effects on the acidity of remote alpine lakes. *Nature, 387*(6628), 64-67. DOI: 10.1038/387064a0

Swinnen, K. R. R., Rutten, A., Nyssen, J., & Leirs, H. (2019). Environmental factors influencing beaver dam locations. *The Journal of Wildlife Management, 83*(2): 356-364. https://doi.org/10.1002/jwmg.21601

Thies, H., Nickus, U., Mair, V., Tessadri, R., Tait, D., Thaler, B., & Psenner, R. (2007). Unexpected Response of High Alpine Lake Waters to Climate Warming. *Environmental Science & Technology, 41*(21), 7424-7429. https://doi.org/10.1021/es0708060

Todd, A. S., Manning, A. H., Verplanck, P. L., Crouch, C., McKnight, D. M., & Dunham, R. (2012). Climate-Change-Driven Deterioration of Water Quality in a Mineralized Watershed. *Environmental Science & Technology, 46*(17), 9324-9332. https://doi.org/10.1021/es3020056

Tuttle, M. L. W., Fahy, J. W., Elliott, J. G., Grauch, R. I., & Stillings, L. L. (2014). Contaminants from Cretaceous black shale: I. Natural weathering processes controlling contaminant cycling in Mancos Shale, southwestern United States, with emphasis on salinity and selenium. *Applied Geochemistry, 46*, 57-71. https://doi.org/10.1016/j.apgeochem.2013.12.010

Vairavamurthy, A. (1998). Using X-ray absorption to probe sulfur oxidation states in complex molecules. *Spectrochimica Acta Part A: Molecular and Biomolecular Spectroscopy, 54*(12), 2009-2017. https://doi.org/10.1016/S1386-1425(98)00153-X

Varadharajan, C., Kakalia, Z., Banfield, J., Berkelhammer, M., Brodie, E., Christianson, D., et al. (2020). [Dataset] Location Identifiers, Metadata, and Map for Field Measurements at the East River Watershed, Colorado, USA. Watershed Function SFA. ESS-DIVE repository. doi:10.15485/1660962

Wan, J., Tokunaga, T. K., Brown, W., Newman, A. W., Dong, W., Bill, M., et al. (2021). Bedrock weathering contributes to subsurface reactive nitrogen and nitrous oxide emissions. *Nature Geoscience, 14*(4), 217-224. https://doi.org/10.1038/s41561-021-00717-0

Westbrook, C. J., Cooper, D.J., Baker, B.W. (2006). Beaver dams and overbank floods influence groundwater–surface water interactions of a Rocky Mountain riparian area. *Water Resources Research 42*(6). https://doi.org/10.1029/2005WR004560

Whitmire, S. L., & Hamilton, S. K. (2005). Rapid Removal of Nitrate and Sulfate in Freshwater Wetland Sediments. *Journal of Environmental Quality, 34*(6), 2062-2071. https://doi.org/10.2134/jeq2004.0483

Wilhelm Scherer, H. (2009). Sulfur in soils. *Journal of Plant Nutrition and Soil Science, 172*(3), 326-335. https://doi.org/10.1002/jpln.200900037

Williams, K. H., Beutler, C., Brown, W., Newman, A., & Versteeg, R. (2020). [Dataset] Anion Data for the East River Watershed, Colorado. Watershed Function SFA, ESS-DIVE repository. doi: 10.15485/1668054

Wiltfong, R., Mitra-Kirtley, S., Mullins, O. C., Andrews, B., Fujisawa, G., & Larsen, J. W. (2005). Sulfur Speciation in Different Kerogens by XANES Spectroscopy. *Energy & Fuels, 19*(5), 1971-1976. https://doi.org/10.1021/ef049753n

Winnick, M. J., Carroll, R. W. H., Williams, K. H., Maxwell, R. M., Dong, W., & Maher, K. (2017). Snowmelt controls on concentration-discharge relationships and the balance of oxidative and acid-base weathering fluxes in an alpine catchment, East River, Colorado. *Water Resources Research, 53*(3), 2507-2523. http://dx.doi.org/10.1002/2016WR019724

Wögrath, S., & Psenner, R. (1995). Seasonal, annual and long-term variability in the water chemistry of a remote high mountain lake: Acid rain versus natural changes. *Water, Air, & Soil Pollution, 85*(2), 359-364. DOI: 10.1007/BF00476855